Trabajo Fin de Máster
Máster Universitario en Ingeniería de Caminos, Canales y Puertos

A 2.5D spectral approach based on the BEM and the FEM to study wave propagation in fluid acoustics and elastodynamics

Autor: Francisco Javier Cruz Muñoz

Tutor: Antonio Romero Ordóñez

Tutor: Pedro Galvín Barrera

Dep. Mecánica de Medios Continuos y Teoría de Estructuras
Escuela Técnica Superior de Ingeniería
Universidad de Sevilla

Sevilla, 2016

Trabajo Fin de Máster
Máster Universitario en Ingeniería de Caminos, Canales y Puertos

A 2.5D spectral approach based on the BEM and the FEM to study wave propagation in fluid acoustics and elastodynamics

Author:
Francisco Javier Cruz Muñoz

Advisors:
Antonio Romero Ordóñez
Pedro Galvín Barrera

Dep. Mecánica de Medios Continuos y Teoría de Estructuras
Escuela Técnica Superior de Ingeniería
Universidad de Sevilla

Sevilla, 2016

Trabajo Fin de Máster: A 2.5D spectral approach based on the BEM and the FEM to study wave propagation in fluid acoustics and elastodynamics

Autor: Francisco Javier Cruz Muñoz
Tutor: Antonio Romero Ordóñez
Pedro Galvín Barrera

El tribunal nombrado para juzgar el trabajo arriba indicado, compuesto por los siguientes profesores:

Presidente:

Vocal/es:

Secretario:

acuerdan otorgarle la calificación de:

El Secretario del Tribunal

Fecha:

Agradecimientos

He aquí mis mas sinceros agradecimientos a todas las personas sin las cuales no habría podido llegar hasta aquí.

A Pedro Galvín y Antonio Romero, por haberme dado la oportunidad de aprender tanto durante el tiempo que hemos compartido y por su inestimable ayuda estos años.

A Cristina Lugo, por ser como es y por estar ahí siempre.

A mi familia y amigos, por el apoyo mostrado a lo largo de la carrera.

A mis compañeros, en breve colegas de la profesión, por haberme hecho el camino hacia la meta más sencillo.

Al resto de profesores de la Escuela Técnica Superior de Ingeniería que han participado de mi formación y propiciado que haya llegado hasta aquí.

Al proyecto BIA2013-43085-P financiado por el Ministerio de Economía y Competitividad en el que está enmarcado este trabajo, y al Centro Informático Cientfico de Andalucia (CICA).

Resumen

En este trabajo se presenta una formulación espectral en dos dimensiones y media (2.5D) basada en el método de los elementos finitos (MEF) y el método de los elementos de contorno (MEC) para estudiar la propagación de ondas en medios acústicos y elásticos en problemas tridimensionales (3D). El análisis se lleva a cabo mediante la superposición de problemas bidimensionales (2D) para diferentes números de onda a lo largo de la coordenada longitudinal. El método numérico está basado en la descomposición del dominio para representar el sistema fluido-estructura. Se presenta en este trabajo un elemento finito espectral para representar ondas guiadas en sólidos con sección transversal arbitraria. Además, el MEC se extiende a la formulación espectral para estudiar medios fluidos infinitos. Ambas aproximaciones utilizan polinomios de interpolación de Lagrage como funciones de forma en los puntos de Legendre-Gauss-Lobatto (LGL). Las técnicas propuestas se han verificado mediante dos problemas de referencia: la propagación de ondas en un medio fluido infinito en presencia de una cavidad rígida fija y la propagación de ondas en un carril libre, y los resultados obtenidos presentan un buen grado de acuerdo con las soluciones de referencia. Se realiza un breve análisis $h-p$ para evaluar la precisión de los métodos.

Abstract

This work presents a two-and-a-half dimensional (2.5D) spectral formulation based on the finite element method (FEM) and the boundary element method (BEM) to study three dimensional (3D) wave propagation in fluid acoustics and elastodynamics. The analysis is carried out by superposing two dimensional (2D) problems for different longitudinal wavenumbers. The numerical method is based on the domain decomposition to study structure-fluid system. A spectral finite element to represent waveguides in solids with arbitrary cross-section is proposed. Moreover, the BEM is extended to its spectral formulation to study unbounded fluid-acoustics media. Both approaches use Lagrange interpolant polynomials as element shape functions at the Legendre-Gauss-Lobatto (LGL) points. The proposed techniques are verified from two benchmark problems: the wave propagation in an unbounded fluid medium in presence of a fixed rigid cavity and the wave propagation in a free rail. The computed results are in good agreement with the reference solution. A brief $h-p$ analysis is done to assess the accuracy of the methods.

Contents

1 Introduction

1.1 Problem outline and motivation

Time-harmonic wave propagation, such as fluid acoustics and solid scattering, is a common phenomenon that appears in many engineering fields. Hybrid methods based on the Boundary Element Method (BEM) and the Finite Element Method (FEM) are suitable to study solid and fluid interaction in unbounded media. The propagation of acoustic waves triggered by static and moving pressure sources, the vibration assessment and the acoustic insulation involve fluid and solid interaction and must be considered rigorously. The finite element method (FEM) have been used is several works to predict the response in fluid-structure interaction problems. For the low frequency range, the conventional finite elements with linear shape represent accurately the fluid and solid scattering waves. However, at high frequencies, these shape functions do not provide reliable results due to so-called pollution effects [1, 14]: the accuracy of the numerical solution deteriorates with increasing non-dimensional wave number and it is not sufficient the commonly employed rules of n elements per wavelength [11]. High element resolutions are required in order to obtain results with reasonable accuracy.

The pollution effect (numerical dispersion) cannot be avoided in two and three dimensional problems [17], but it can be reduced by using higher order shape functions. Ihlenburg and Babuška [12, 13] demonstrates that the numerical dispersion of FEM for Helmholtz equation is related to the stability of the Helmholtz differential operator at high wavenumber. Moreover, high-order numerical formulation improves the accuracy of the numerical method in order to reduce the dimensions of the discretisation. Deraemaeker et al. [8] studied several finite element methodologies for the Helmholtz equation. They concluded that the p-FEM drastically reduces the pollution error. Mehdizadeh and Paraschivoiu [16] compared a Spectral Element Method (SEM) and a second-order FEM. The authors concluded that the two-dimensional SEM leads to fewer number of elements per wavelength and less computational cost, in terms of both memory and computational time, for the same accuracy. Vos et al. [23] presented an efficient implementation of a spectral$/h-p$ element method and they analysed which specific combination of mesh size h and polynomial order p minimises the computational cost to solve a problem up to a predefined level of accuracy for smooth and non-smooth solutions. In the $h-p$ method the integration is usually done by numerical integration which can induce numerical error [2].

The SEM is close to the p-FEM [18], and handles some of the advantages regarding the representation of non-homogeneity properties. The studied domain is discretized into elements and the field variable is usually represented with high-order interpolation shape function through the integration points. The p-FEM and spectral methodologies have been developed using several shape function families: Lagrange, Legendre and Bernstein polynomials. Biermann et al. [5] and Petersen et al. [19] studied several shape functions families for acoustic simulations. They concluded regarding the simulation of acoustic phenomena, governed by the Helmholtz equation, that the high-order finite elements are an efficient method even in the higher frequency range, and the elements based on Bernstein polynomials provided the most efficient and stable solution procedure for the analysed problems. Bériot et al. [4] compared several polynomial bases commonly used in FEM and SEM for controlling the pollution and to lead to more efficient technique for convected wave propagation problems. The authors concluded that the properties of p-FEM that make its strength for standard acoustics remain for flow acoustics as well. At high wave numbers, where the dispersion error was

likely to dominate the total numerical error, *p*-FEM elements proved to efficiently mitigate the pollution effect also for convected applications.

Many authors have successfully applied the spectral element method in different fields. Degrande and De Roeck [7] developed a high-order method for studying the dynamic response of a porous saturated medium using spectral elements. They use as shape functions, in a displacement formulation, the analytical solution for Biot equations restricted to two-dimensional (2D) plane strain wave propagation. Bar-Yoseph et al. [3] presented a space-time spectral element method to solve a simply supported modified Euler-Bernoulli beam undergoing external forced lateral vibrations. They examined two Galerkin formulations using Hermitian and Lagrangian polynomials as interpolants for spatial and time discretisations. The space-time SEM allows the use of larger time steps while maintaining the accuracy of the solution. Kudela et al. [15] applied spectral finite elements for studying the wave propagation in an isotropic rod and in a Timoshenko beam. The authors proposed this methodology to detect small damage in structures. The computed results were compared to those obtained from the classical FEM and from measurements. This comparison highlighted the efficiency of the spectral elements and it confirms that the methodology reflects this phenomenon quite well. Zhu et al. [24] coupled Chebyshev spectral elements with the implicit Newmark time integral method to simulate acoustic field. The presented results indicated that the accuracy increased as the time step decreased. The result of this study also concluded that uniform distribution of node is better for the improvement of numerical accuracy.

1.2 Objetives

The method proposed in this work regards with a two-and-a-half dimensional (2.5D) approach to represent fluid-solid interaction (FSI) problems. The study of three-dimensional (3D) scattered waves in fluid and solid media requires the use of highly computational demanding models. The solution becomes much simpler if the medium is homogeneous in one direction, even if the dynamic source remains 3D. Such situation is referred to as a two-and-a-half dimensional problems [6]. This work proposes a 2.5D spectral formulation based on the FEM and the BEM to study wave propagation in fluid-structure interaction problems. The proposed approach is useful for problems where the material and geometric properties are uniform along one direction, and the source exhibits 3D behaviour.

1.3 Original contributions

The following points give an outline of what are perceived to be the significant contributions from the present work.

- The boundary element method in 2.5D in fluid acoustics has been extended to its spectral formulation to allow for the computation of wave propagation problems in fluid media. This introduces a new accurate method, with lower computational efforts, to solve problems at a higher frequency range.
- Moreover, a new 2.5D spectral finite element is presented to study solid waveguides.

1.4 Organization of the text

The outline of this work is as follows. First, the numerical model is presented. The spectral finite elements formulation in elastodynamics is described. Then, the spectral boundary elementh method in fluid acoustics is discused. Finally, the proposed methods are then verified with two benchmark problems [20, 10].

2 Numerical model

The spectral formulation is based on a 2.5D coupled BEM-FEM formulation, where the solid (Ω_s) is represented by the FEM, while the limiting interface (Γ_f) between the solid and the fluid ($\Omega_{f\infty}$) is modelled with the BEM (Figure 2.1). In this work both formulations have been developed separately and the coupling procedure is a line of a future research.

The 2.5D formulation computes the problem solution as the superposition of two-dimensional (2D) problems with a different longitudinal wavenumber, k_z, in the z direction. An inverse Fourier transform is used to compute the 3D solution:

$$a(\mathbf{x},\omega) = \int_{-\infty}^{+\infty} \widehat{a}(\widehat{\mathbf{x}},k_z,\omega)e^{-ik_z z}dk_z \tag{2.1}$$

where $a(\mathbf{x},\omega)$ is the unknown magnitude (e.g., displacement or pressure), $\widehat{a}(\widehat{\mathbf{x}},k_z,\omega)$ is its representation in the frequency-wavenumber domain, $\widehat{\mathbf{x}} = \mathbf{x}(x,y,0)$, ω is the angular frequency, and $i = \sqrt{-1}$. The integral defined by Equation (2.1) is transformed into a summation as follows:

$$a(\mathbf{x},\omega) = \sum_{-\infty}^{+\infty} \widehat{a}(\widehat{\mathbf{x}},k_z,\omega)e^{-ik_z z}\Delta k_z \tag{2.2}$$

with $k_z = m\Delta k_z$. This equation converges and can be aproximated by a finite sum of terms.

2.1 The 2.5D spectral boundary element formulation

The boundary element formulation presented in this work considers an arbitrary boundary submerged in an unbounded fluid medium. The integral representation of the pressure p^i for a point i located at the fluid subdomain $\Omega_{f\infty}$, with zero body forces and zero initial conditions may be written as [9]:

$$c^i p^i(\mathbf{x}^i,\omega) = \int_{\Gamma_f} p^{i*}(\mathbf{x},\omega;\mathbf{x}^i)u^i(\mathbf{x},\omega)d\Gamma - \int_{\Gamma_f} u^{i*}(\mathbf{x},\omega;\mathbf{x}^i)p^i(\mathbf{x},\omega)d\Gamma \tag{2.3}$$

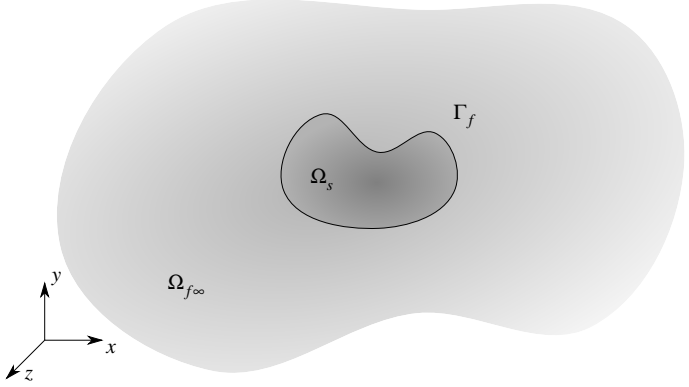

Figure 2.1 Domain decomposition.

where $u^i(\mathbf{x},\omega)$ and $p^i(\mathbf{x},\omega)$ are respectively the normal displacement to boundary Γ_f and the nodal pressure. $u^{i*}(\mathbf{x},\omega;\mathbf{x}^i)$ and $p^{i*}(\mathbf{x},\omega,\mathbf{x}^i)$ are respectively the fluid full-space fundamental solution for normal displacement and pressure at point $\mathbf{x}$ due to a point load at $\mathbf{x}^i$. The integral-free term c^i depends only on the boundary geometry at point i. The integration boundary Γ_f represents the boundary between the unbounded fluid medium ($\Omega_{f\infty}$) and the solid subdomain (Ω_s).

Assuming that the unbounded medium is constant in the longitudinal direction z, Equation (2.3) is expressed in terms of integrals in this direction and over the cross-section boundary, Σ_f:

$$c^i p^i(\mathbf{x},\omega) = \int_{-\infty}^{+\infty}\int_{\Sigma_f} p^{i*}(\mathbf{x},\omega;\mathbf{x}^i)u^i(\mathbf{x},\omega)dSdz - \int_{-\infty}^{+\infty}\int_{\Sigma_f} u^{i*}(\mathbf{x},\omega;\mathbf{x}^i)p^i(\mathbf{x},\omega)dSdz \tag{2.4}$$

Equation (2.4) is then transformed to the wavenumber domain as:

$$c^i \widehat{p}^i(\widehat{\mathbf{x}},\omega,k_z) = \int_{\Sigma_f} \widehat{p}^{i*}(\widehat{\mathbf{x}},\omega,k_z;\widehat{\mathbf{x}}^i)\widehat{u}^i(\widehat{\mathbf{x}},\omega,k_z)dS - \int_{\Sigma_f} \widehat{u}^{i*}(\widehat{\mathbf{x}},\omega,k_z;\widehat{\mathbf{x}}^i)\widehat{p}^i(\widehat{\mathbf{x}},\omega,k_z)dS \tag{2.5}$$

where a hat above a variable denotes its representation in the frequency-wavenumber domain.

The problem is discretised into elements, leading to a boundary approximation of the normal displacement and pressure using the interpolation shape functions $\boldsymbol{\phi}^j$. Then, Equation (2.5) is written as:

$$c^i\widehat{p}^i = \sum_{j=1}^{Q}\left[\left\{\int_{\Sigma_f^j}\widehat{p}^{i*}\boldsymbol{\phi}^j d\Sigma\right\}\widehat{u}^i - \left\{\int_{\Sigma_f^j}\widehat{u}^{i*}\boldsymbol{\phi}^j d\Sigma\right\}\widehat{p}^i\right] = \sum_{j=1}^{Q}\left[\widehat{\mathbf{H}}^{ij}\widehat{u}^i - \widehat{\mathbf{G}}^{ij}\widehat{p}^i\right] \tag{2.6}$$

where Q is the number of boundary nodes at the boundary Σ_f and Σ_f^j are the elements which contains the node j. After interpolating the boundary variables, the integral representation defined by Equation (2.6) yields a system of equations that is solved for each frequency.

The spatial integrations in Equation (2.6) are numerically evaluated by a Lobatto-Gauss-Legendre (LGL) quadrature when the collocation point does not belong to the integration element. In a first approach, a LGL quadrature is also used to evaluate the singular integrals when the collocation point belongs to the integration element using an appropiate number of integration points. References [21, 22] state that the use of a sufficient number of quadrature points leads to a good approximation of the singular integrals.

The system of equations for all the boundary elements becomes:

$$\widehat{\mathbf{H}}(\omega,k_z)\widehat{u}(\widehat{\mathbf{x}},\omega,k_z) = \widehat{\mathbf{G}}(\omega,k_z)\widehat{p}(\widehat{\mathbf{x}},\omega,k_z) \tag{2.7}$$

The proposed spectral boundary element method for the 2.5D fluid element uses Legendre polynomials of order p as interpolation shape functions. The shape interpolation functions $\boldsymbol{\phi}$ are given by:

$$\phi_i = \prod_{j\neq i}\frac{\xi-\xi_i}{\xi_j-\xi_i} \tag{2.8}$$

where the local nodal coordinates ξ are found at the LGL integration points:

$$(1-\xi^2)\frac{\partial\boldsymbol{\phi}(\xi)}{\partial\xi} = 0 \tag{2.9}$$

The element integration is carried out using the LGL points. Then, the computation of matrices $\widehat{\mathbf{H}}$ y $\widehat{\mathbf{G}}$ is simplified as follows:

$$\begin{aligned}\widehat{h}_{ij} &= \widehat{p}^{i*}(\widehat{\mathbf{x}},\omega,k_z;\widehat{\mathbf{x}^i})w_j\left|\mathbf{J}(\xi_j)\right| \\ \widehat{g}_{ij} &= \widehat{u}^{i*}(\widehat{\mathbf{x}},\omega,k_z;\widehat{\mathbf{x}^i})w_j\left|\mathbf{J}(\xi_j)\right|\end{aligned} \tag{2.10}$$

where w_j is the LGL integration weight at the natural nodal coordinate ξ_j, and $\left|\mathbf{J}(\xi_j)\right|$ is the Jacobian evaluated at ξ_j, $\widehat{u}^{i*}(\widehat{\mathbf{x}},\omega,k_z;\widehat{\mathbf{x}^i})$ and $\widehat{p}^{i*}(\widehat{\mathbf{x}},\omega,k_z;\widehat{\mathbf{x}^i})$ are respectively normal displacement to boundary Γ_f and nodal pressure, and both are derived from a potential:

$$\begin{aligned}\widehat{u}^{i*}(\widehat{\mathbf{x}},\omega,k_z;\widehat{\mathbf{x}^i}) &= -\tfrac{i}{4}H_1^{(2)}(k_\alpha r)\tfrac{\partial r}{\partial\mathbf{n}} \\ \widehat{p}^{i*}(\widehat{\mathbf{x}},\omega,k_z;\widehat{\mathbf{x}^i}) &= \tfrac{i}{4}H_0^{(2)}(k_\alpha r)\end{aligned} \tag{2.11}$$

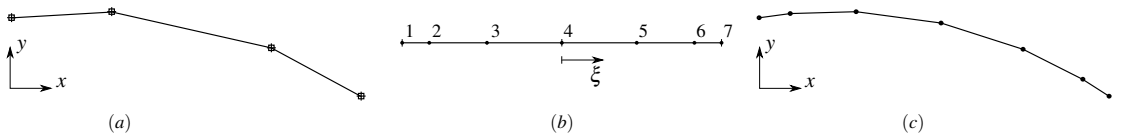

Figure 2.2 (a) Element mesh seed representation, (b) element definition and (c) physical representation of spectral fluid boundary element of order $p = 6$.

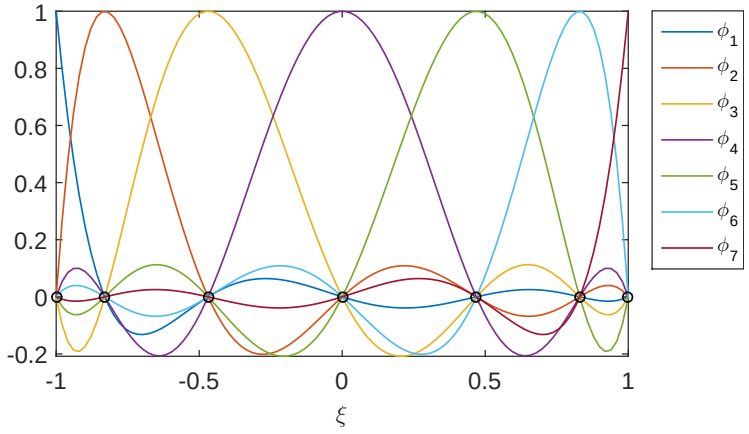

Figure 2.3 Element shape functions for an element with order $p = 6$.

where $H_n^{(2)}$ are second Hankel funtions of order n, $k_\alpha = \sqrt{\frac{\omega^2}{\alpha^2} - k_z^2}$, with $\mathrm{Im}(k_\alpha) < 0$, α is the sound propagation velocity and $r = \sqrt{(x-x_0)^2 + (y-y_0)^2}$.

The boundary Γ_f is discretized into elements that are generated from a base mesh. The element definition is done by using a polynomial interpolation from the element base mesh and its representation in the natural coordinates system. As an example, Figure 2.2.(a) shows an element base mesh defined by four nodes used to generate an element with order $p = 6$ (Figure 2.2.(c)). The spectral element nodes are defined in natural coordinates in ascending order (Figure 2.2.(b)) with $\xi \in [-1,1]$.

The shape function $\boldsymbol{\phi}$ and its derivatives are symbolically computed in straightforward procedure for an arbitrary element order. Figure 2.3 shows the interpolation shape functions for the $p = 6$ spectral element presented in Figure 2.2.

2.2 The 2.5D spectral finite element formulation

The spectral formulation for solid subdomains is based on the virtual work principle. For any virtual displacement field $\delta\mathbf{u}$ imposed on the solid subdomain Ω_s, the virtual work due to the internal and the inertial forces must be equal to the virtual work produced by the external loads [25]:

$$\begin{aligned} &-\omega^2 \int_{\Omega_s} \delta\mathbf{u}(\mathbf{x},\omega)\rho_s\mathbf{u}(\mathbf{x},\omega)d\Omega + \int_{\Omega_s} \delta\boldsymbol{\varepsilon}(\mathbf{x},\omega)\boldsymbol{\sigma}(\mathbf{x},\omega)d\Omega \\ &= \int_{\Omega_s} \delta\mathbf{u}(\mathbf{x},\omega)\rho_s\mathbf{b}(\mathbf{x},\omega)d\Omega + \int_{\Gamma_s} \delta\mathbf{u}(\mathbf{x},\omega)\mathbf{f}(\mathbf{x},\omega)d\Gamma \end{aligned} \tag{2.12}$$

where $\mathbf{u}(\mathbf{x},\omega)$ is the displacement vector, $\boldsymbol{\varepsilon}$ and $\boldsymbol{\sigma}$ are respectively the strain and stress tensors, $\rho_s\mathbf{b}(\mathbf{x},\omega)$ is the body force in the domain Ω_s, ρ_s is the solid density, and $\mathbf{f}(\mathbf{x},\omega)$ is the nodal force vector. A variable preceded by δ denotes a virtual change of its magnitude.

The Voigt notation is used to write both the symmetrical stress tensor $\boldsymbol{\sigma}$ and the strain tensor $\boldsymbol{\varepsilon}$, $\boldsymbol{\sigma} = \{\sigma_{xx},\sigma_{yy},\sigma_{zz},\sigma_{xy},\sigma_{yz},\sigma_{zx}\}^T$ and $\boldsymbol{\varepsilon} = \{\varepsilon_{xx},\varepsilon_{yy},\varepsilon_{zz},\gamma_{xy},\gamma_{yz},\gamma_{zx}\}^T$, respectively. The use of engineering shear strains allows to write the internal work as an inner product $\varepsilon_b^T\sigma_b$.

The displacement vector $\mathbf{u}(\mathbf{x},\omega)$ is discretized as:

$$\mathbf{u}(\mathbf{x},\omega) = \mathbf{N}\underline{\mathbf{u}}(\mathbf{x},\omega) \tag{2.13}$$

where $\mathbf{N}$ are the globally defined shape functions and $\underline{\mathbf{u}}(\mathbf{x},\omega)$ is the nodal displacement vector.

The strain tensor $\boldsymbol{\varepsilon}$ is derived from the nodal displacement vector $\underline{\mathbf{u}}(\mathbf{x},\omega)$ as:

$$\boldsymbol{\varepsilon} = \mathbf{L}_1\mathbf{N}\underline{\mathbf{u}} + \mathbf{L}_2\mathbf{N}\frac{\partial \underline{\mathbf{u}}}{\partial z} \tag{2.14}$$

where

$$\mathbf{L}_1 = \begin{bmatrix} \frac{\partial}{\partial x} & 0 & 0 \\ 0 & \frac{\partial}{\partial y} & 0 \\ 0 & 0 & 0 \\ \frac{\partial}{\partial y} & \frac{\partial}{\partial x} & 0 \\ 0 & 0 & \frac{\partial}{\partial y} \\ 0 & 0 & \frac{\partial}{\partial x} \end{bmatrix} \tag{2.15}$$

and

$$\mathbf{L}_2 = \begin{bmatrix} 0 & 0 & 0 \\ 0 & 0 & 0 \\ 0 & 0 & 1 \\ 0 & 0 & 0 \\ 0 & 1 & 0 \\ 1 & 0 & 0 \end{bmatrix} \tag{2.16}$$

The strain vector $\boldsymbol{\varepsilon}$ in Equation (2.14) is related to both the displacement vector $\underline{\mathbf{u}}$ and its derivative $\partial\underline{\mathbf{u}}/\partial z$ with respect to the longitudinal coordinate z. This differs from the relationship $\boldsymbol{\varepsilon} = \mathbf{L}\mathbf{N}\underline{\mathbf{u}}$ for the 3D formulation, where the strain vector is written as a linear combination of the elements of the nodal displacement vector $\underline{\mathbf{u}}$. Equation (2.14) is alternatively written as:

$$\boldsymbol{\varepsilon} = \mathbf{B}_1\underline{\mathbf{u}} + \mathbf{B}_2\frac{\partial \underline{\mathbf{u}}}{\partial z} \tag{2.17}$$

where $\mathbf{B}_1 = \mathbf{L}_1\mathbf{N}$ and $\mathbf{B}_2 = \mathbf{L}_2\mathbf{N}$.

The stress tensor is related to the strain vector through the constitutive relation:

$$\boldsymbol{\sigma} = \mathbf{D}\boldsymbol{\varepsilon} \tag{2.18}$$

where, in the case of a linear isotropic material, the constitutive matrix $\mathbf{D}$ depends on the Young's modulus E and the Poisson's ratio ν:

$$\mathbf{D} = \frac{E}{(1+\nu)(1-2\nu)} \begin{bmatrix} 1-\nu & \nu & \nu & 0 & 0 & 0 \\ \nu & 1-\nu & \nu & 0 & 0 & 0 \\ \nu & \nu & 1-\nu & 0 & 0 & 0 \\ 0 & 0 & 0 & \frac{1-2\nu}{2} & 0 & 0 \\ 0 & 0 & 0 & 0 & \frac{1-2\nu}{2} & 0 \\ 0 & 0 & 0 & 0 & 0 & \frac{1-2\nu}{2} \end{bmatrix} \tag{2.19}$$

A standard Galerkin procedure is followed, using the same approximation for the virtual displacement vector. Substituting the strain-displacement relation defined by Equation (2.17), and the constitutive Equation (2.18) into the virtual work Equation (2.12) yields:

$$\begin{aligned} &-\omega^2 \int_{\Omega_s} \delta\underline{\mathbf{u}}^T \mathbf{N}^T \rho_s \mathbf{N}\underline{\mathbf{u}}\, d\Omega + \int_{\Omega_s} \left(\delta\underline{\mathbf{u}}^T \mathbf{B}_1^T + \delta \left(\frac{\partial \underline{\mathbf{u}}}{\partial z} \right)^T \mathbf{B}_2^T \right) \mathbf{D} \left(\mathbf{B}_1\underline{\mathbf{u}} + \mathbf{B}_2 \frac{\partial \underline{\mathbf{u}}}{\partial z} \right) d\Omega \\ &= \int_{\Omega_b} \delta\underline{\mathbf{u}}^T \mathbf{N}^T \rho_s \mathbf{b}\, d\Omega + \int_{\Gamma_f} \delta\underline{\mathbf{u}} \mathbf{N}^T \mathbf{f}\, d\Gamma \end{aligned} \tag{2.20}$$

Equation (2.20) is further elaborated, rewriting the volume integrals over the longitudinal coordinate z and the cross-section A_s:

$$\begin{aligned}
&-\omega^2 \int_{-\infty}^{\infty} \delta\underline{\mathbf{u}}^T \left(\int_{A_s} \mathbf{N}^T \rho_s \mathbf{N} dA \right) \underline{\mathbf{u}} dz + \int_{-\infty}^{\infty} \delta\underline{\mathbf{u}}^T \left(\int_{A_s} \mathbf{B}_1^T \mathbf{D} \mathbf{B}_1 dA \right) \underline{\mathbf{u}} dz \\
&+ \int_{-\infty}^{\infty} \delta\underline{\mathbf{u}}^T \left(\int_{A_s} \mathbf{B}_1^T \mathbf{D} \mathbf{B}_2 dA \right) \frac{\partial \underline{\mathbf{u}}}{\partial z} dz + \int_{-\infty}^{\infty} \delta \left(\frac{\partial \underline{\mathbf{u}}}{\partial z} \right)^T \left(\int_{A_s} \mathbf{B}_2^T \mathbf{D} \mathbf{B}_1 dA \right) \underline{\mathbf{u}} dz \\
&+ \int_{-\infty}^{\infty} \delta \left(\frac{\partial \underline{\mathbf{u}}}{\partial z} \right)^T \left(\int_{A_s} \mathbf{B}_2^T \mathbf{D} \mathbf{B}_2 dA \right) \frac{\partial \underline{\mathbf{u}}}{\partial z} dz \\
&= \int_{-\infty}^{\infty} \delta\underline{\mathbf{u}}^T \left(\int_{A_s} \mathbf{N}^T \rho_s \mathbf{b} dA \right) dz + \int_{-\infty}^{\infty} \delta\underline{\mathbf{u}}^T \left(\int_{\Sigma_f} \mathbf{N}^T \mathbf{f} d\Sigma \right) dz
\end{aligned} \tag{2.21}$$

where Σ_f is the intersection of the surface Γ_f with the plane $z = 0$ (Figure 2.1). The discretized equation is obtained through elimination of the virtual displacement vector $\delta\underline{\mathbf{u}}$. This requires integration by parts on the terms containing derivatives $\delta\left(\partial\underline{\mathbf{u}}/\partial z\right)$ in Equation (2.21):

$$\begin{aligned}
&-\omega^2 \int_{-\infty}^{\infty} \delta\underline{\mathbf{u}}^T \left[\int_{A_s} \mathbf{N}^T \rho_s \mathbf{N} dA \right] \underline{\mathbf{u}} dz + \int_{-\infty}^{\infty} \delta\underline{\mathbf{u}}^T \left[\int_{A_s} \mathbf{B}_1^T \mathbf{D} \mathbf{B}_1 dA \right] \underline{\mathbf{u}} dz \\
&+ \int_{-\infty}^{\infty} \delta\underline{\mathbf{u}}^T \left[\int_{A_s} \mathbf{B}_1^T \mathbf{D} \mathbf{B}_2 dA - \int_{A_s} \mathbf{B}_2^T \mathbf{D} \mathbf{B}_1 dA \right] \frac{\partial \underline{\mathbf{u}}}{\partial z} dz \\
&- \int_{-\infty}^{\infty} \delta\underline{\mathbf{u}}^T \left(\int_{A_s} \mathbf{B}_2^T \mathbf{D} \mathbf{B}_2 dA \right) \frac{\partial^2 \underline{\mathbf{u}}}{\partial z^2} dz \\
&= \int_{-\infty}^{\infty} \delta\underline{\mathbf{u}}^T \left(\int_{A_s} \mathbf{N}^T \rho_s \mathbf{b} dA \right) dz + \int_{-\infty}^{\infty} \delta\underline{\mathbf{u}}^T \left(\int_{\Sigma_f} \mathbf{N}^T \mathbf{f} d\Sigma \right) dz
\end{aligned} \tag{2.22}$$

Since Equation (2.22) holds for any virtual displacement $\delta\underline{\mathbf{u}}$, all integrals over the longitudinal coordinate z vanish and Equation (2.22) is written as follows:

$$-\omega^2 \mathbf{M} \underline{\mathbf{u}} + \mathbf{K}^0 \underline{\mathbf{u}} + \mathbf{K}^1 \frac{\partial \underline{\mathbf{u}}}{\partial z} + \mathbf{K}^2 \frac{\partial^2 \underline{\mathbf{u}}}{\partial z^2} = \underline{\mathbf{f}} \tag{2.23}$$

where the mass matrix $\mathbf{M}$ is defined as:

$$\mathbf{M} = \int_{A_s} \mathbf{N}^T \rho_s \mathbf{N} dA \tag{2.24}$$

and stiffness matrices $\mathbf{K}^0$, $\mathbf{K}^1$ and $\mathbf{K}^2$ are defined as:

$$\begin{aligned}
\mathbf{K}^0 &= \int_{A_s} \mathbf{B}_1^T \mathbf{D} \mathbf{B}_1 dA \\
\mathbf{K}^1 &= \int_{A_s} \left(\mathbf{B}_1^T \mathbf{D} \mathbf{B}_2 - \mathbf{B}_2^T \mathbf{D} \mathbf{B}_1 \right) dA \\
\mathbf{K}^2 &= \int_{A_s} \mathbf{B}_2^T \mathbf{D} \mathbf{B}_2 dA
\end{aligned} \tag{2.25}$$

The external load vector:

$$\underline{\mathbf{f}} = \int_{A_s} \mathbf{N}^T \rho_s \mathbf{b}(x,y,z,\omega) dA + \int_{\Sigma_f} \mathbf{N}^T \mathbf{f}(x,y,z,\omega) d\Sigma \tag{2.26}$$

contains contributions for both body forces and surface loads and it is evaluated for every point z along the longitudinal axis.

The differential Equation (2.23) is solved by a Fourier transform of the longitudinal coordinate z to the horizontal wavenumber k_z, where the Fourier transform is defined as $\mathscr{F}\left[f(z), k_z\right] = \int_{-\infty}^{\infty} \exp(+ik_z z) f(z) dz$. Equation (2.23) is transformed to the wavenumber domain as:

$$\left[-\omega^2 \mathbf{M} + \mathbf{K}^0 - ik_z \mathbf{K}^1 - k_z^2 \mathbf{K}^2 \right] \widehat{\underline{\mathbf{u}}}(k_z, \omega) = \widehat{\underline{\mathbf{f}}}(k_z, \omega) \tag{2.27}$$

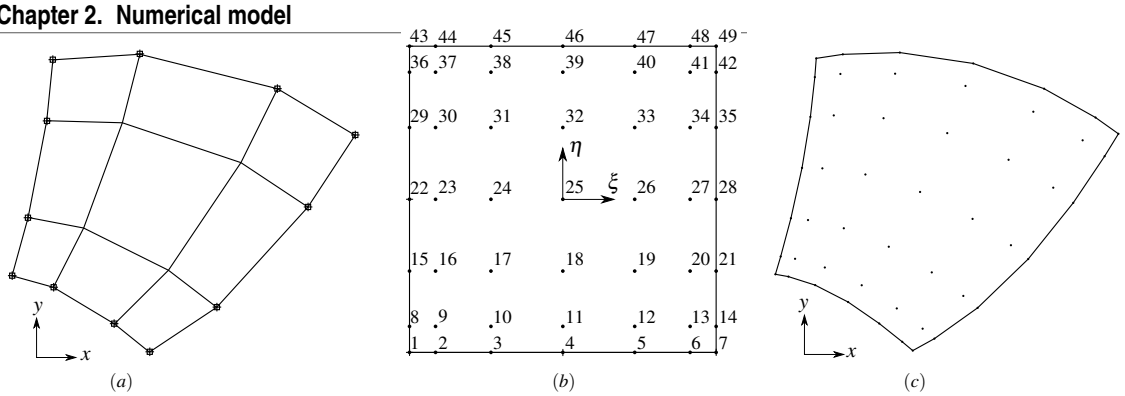

Figure 2.4 (a) Element mesh seed representation, (b) element definition and (c) physical representation of a solid spectral element of order $p = 6$.

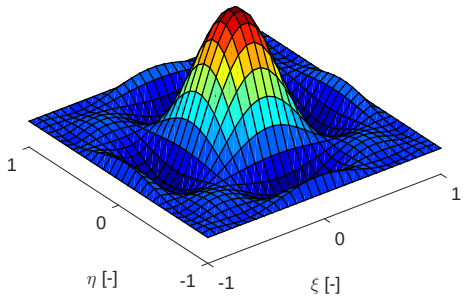

Figure 2.5 Element shape function of $p = 6$ N_{25} for solid finite element.

where a hat above a variable denotes its representation in the frequency-wavenumber domain.

Equation (2.27) is rewritten if an equivalent dynamic stiffness matrix $\widehat{\mathbf{K}}$ is considered:

$$\widehat{\mathbf{K}}(k_z,\omega)\widehat{\underline{\mathbf{u}}}(\widehat{\mathbf{x}},k_z,\omega) = \widehat{\underline{\mathbf{f}}}(\widehat{\mathbf{x}},k_z,\omega) \tag{2.28}$$

where the dynamic stiffness matrix $\widehat{\mathbf{K}}$ is easily computed for each wavenumber and frequency step.

The proposed spectral finite element method uses the 2D Legendre polynomials of order p as specific shape functions $\mathbf{N}$, and the local nodal element coordinates $\boldsymbol{\xi}(\xi,\eta) \in [-1,1]$ x $[-1,1]$ are defined as the Lobatto-Gauss-Legendre (LGL) points:

$$\begin{cases} (1-\xi^2)\frac{\partial \mathbf{N}(\xi,\eta)}{\partial \xi} = 0 \\ (1-\eta^2)\frac{\partial \mathbf{N}(\xi,\eta)}{\partial \eta} = 0 \end{cases} \tag{2.29}$$

Then, the local nodal element coordinate matches the LGL integration points, and defines an orthogonal element shape function basis. Therefore, the solid element matrices defined by Equations (2.24) and (2.25) are easily computed as follows:

$$\begin{aligned} m_{ij} &= \delta_{ij}\rho w_{ij}\left|\mathbf{J}(\xi_i,\eta_j)\right| \\ k^2_{ij} &= \delta_{ij}\mathbf{L}_2^T\mathbf{D}\mathbf{L}_2 w_{ij}\left|\mathbf{J}(\xi_i,\eta_j)\right| \end{aligned} \tag{2.30}$$

where δ_{ij} is the Kronecker delta, w_{ij} is the LGL weight at the nodal coordinate system (ξ_i,η_j), and $\left|\mathbf{J}(\xi_i,\eta_j)\right|$ is the Jacobian evaluated at (ξ_i,η_j).

The solid subdomain Ω_s is discretized into elements that are generated from a base element mesh. The element definition is done by using a polynomial interpolation from the starting element geometry and its representation in the natural coordinates system. As an example, Figure 2.4. shows an element with order $p = 6$. The element nodes are defined in natural coordinates in ascending order (Figure 2.4.(b)) with $\boldsymbol{\xi}(\xi,\eta) \in [-1,1] \times [-1,1]$. The spectral solid element has three degrees of freedom at each node, $\widehat{u}(\widehat{\mathbf{x}},k_z,\omega) = \{\widehat{u}_x(\widehat{\mathbf{x}},k_z,\omega),\widehat{u}_y(\widehat{\mathbf{x}},k_z,\omega),\widehat{u}_z(\widehat{\mathbf{x}},k_z,\omega)\}$.

The element shape functions are computed as $\mathbf{N}_k = \boldsymbol{\phi}_i(\xi)\boldsymbol{\phi}_j(\eta)$, where k is the element node in which the shape function takes unity value, $k = (i-1)(p+1)+j$, and $\boldsymbol{\phi}_i$ is the one-dimensional LGL shape function defined by Equation (2.8). The shape function $\mathbf{N}_k$ and its derivatives are symbolically computed in straightforward procedure for an arbitrary element order. Figure 2.5 shows the interpolation shape function $\mathbf{N}_{25}$ for an spectral element with order $p = 6$ (Figure 2.4.(b)).

3 Numerical verification

The proposed spectral boundary and finite element methods were verified with two benchmark problems regarding to a fixed cylindrical inclusion in an unbounded fluid medium and the propagation of elastic waves in free rail.

3.1 Fixed cylindrical inclusion

The BEM model was verified with a benchmark problem. The model was implemented and validated by applying it to a fixed cylindrical circular cavity, submerged in a homogeneous unboundend fluid medium. The cavity is subjected to a harmonic point pressure load. The analytical solution to this problem can be found in Reference [20].

The cavity has a radius $r = 5\,\mathrm{m}$, and the unbounded fluid medium properties are pressure wave velocity $\alpha = 1500\,\mathrm{m/s}$ and density $\rho = 1000\,\mathrm{kg/m^3}$.

The problem was solved for a frequency range varying from 2.5 Hz to 320 Hz, with a frequency step $\Delta f = 2.5\,\mathrm{Hz}$. A constant value of $k_z = 10^{-5}\,\mathrm{rad/m}$ was assumed. The problem solution was computed directly from Equation (2.7), and then the radiated wave field at receivers was assessed using the Somigliana identity [9].

The problem solution was computed for a dilatational point source placed at the fluid medium $\widehat{\mathbf{x}}_0 = (x_0,y_0) = (0,15)$ 15 m away from the cavity centre. This loads emits a harmonic incident field $\widehat{p}_{inc}$ at a point $\widehat{\mathbf{x}}$ described by:

$$\widehat{p}_{inc} = (\widehat{\mathbf{x}},\omega,k_z) = \frac{-iA}{2} H_0^{(2)}(k_\alpha \sqrt{(x-x_0)^2+(y-y_0)^2}) \tag{3.1}$$

where A is the source amplitude, $H_n^{(2)}$ are the second Hankel functions of order n and $k_\alpha = \sqrt{\frac{\omega^2}{\alpha^2} - k_z^2}$ is the effective wavenumber $(\mathrm{Im}\{k_p\} = 0)$.

The element size and the approximation order was set to keep the nodal density per wavelength at least $d_\lambda = 12$ [4]. The characteristic problem wavelength was $\lambda_{min} = \alpha / f_{max} = 4.69$ m, so to accomplish the above condition the minimum number of nodes must be 80. Three different boundary discretization were investigated for characteristic element distribution $1/h = 2/\pi\ \mathrm{m}^{-1}$, $1/h = 3/\pi\ \mathrm{m}^{-1}$ and $1/h = 4/\pi\ \mathrm{m}^{-1}$. In this study, the element order is $p = 5$. As an example, Figure 3.1 shows a boundary discretization using $1/h = 2/\pi\ \mathrm{m}^{-1}$ and $p = 5$.

The scattered wave field was computed over a grid of receivers as shown in Figure 3.2.

Figure 3.3 shows the amplitude of the analytical solution of the scattered pressure field when acts a harmonic pressure load of 200 Hz and the total incident fields. The maximum amplitude was found near to the source point, and a shadowed region appeared after the cavity.

Figure 3.4 represents the difference between the analytical solution and computed results when the inclusion is modelled with a different number of boundary elements. Maximum errors occur in the shadowed zone and around the surface inclusion. The improvement of the computed solution as the distance to the surface of the cavity increases is noticeable. As expected, the boundary element method accuracy improves as element size decreases. The results showed that higher order elements or small element size must be used to compute the solution at points close to the cavity boundary, where the scattered field changes rapidly.

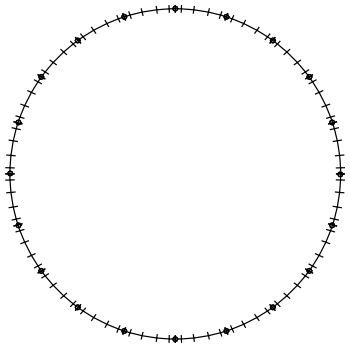

Figure 3.1 Cylindrical cavity embedded in an unbounded fluid medium: problem discretization with element distribution $1/h = 2/\pi$ and order $p = 6$.

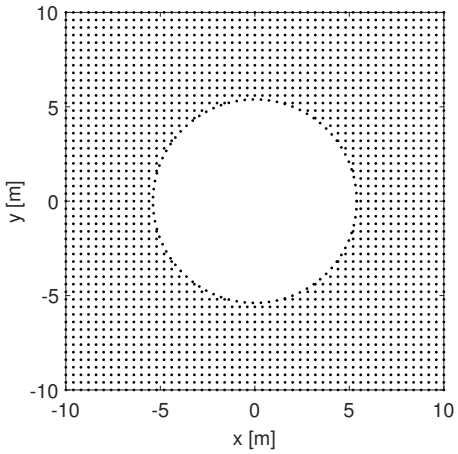

Figure 3.2 Receivers grid.

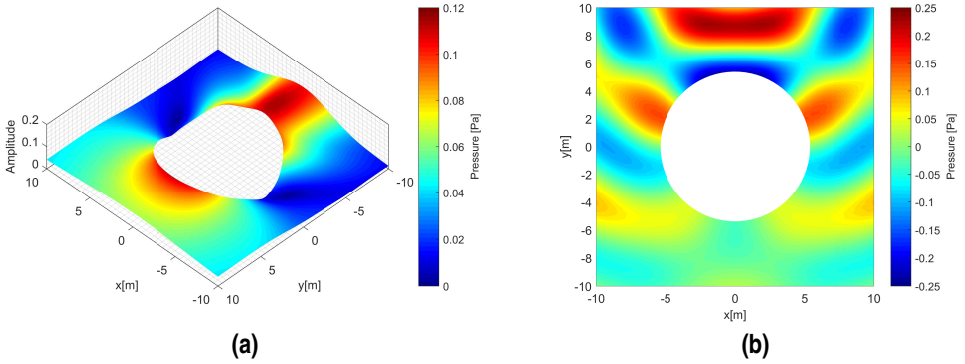

Figure 3.3 (a) Scattered pressure field and (b) total pressure field due to a harmonic pressure load acting at 200 Hz.

3.2 Propagative waves in a free rail

The solid spectral element presented in Section 2.1 was verified through computing of propagative waves in a free rail UIC861-3. This problem was previously studied by L. Gavric [10]. The dispersion curves and the cross-section modes were computed for the wavenumber range $0-35$ rad/m, with a wavenumber step $\Delta k_z = 0.05$ rad/m.

First, the problem was solved using linear finite elements with two different discretizations. The first mesh consists of 227 nodes and 176 finite elements, which results in a mesh of 681 degrees of freedom (Figure 3.5.(a)). The element size varies from $h = 5.7$ mm to $h = 8.6$ mm. This mesh is similar to the mesh used in

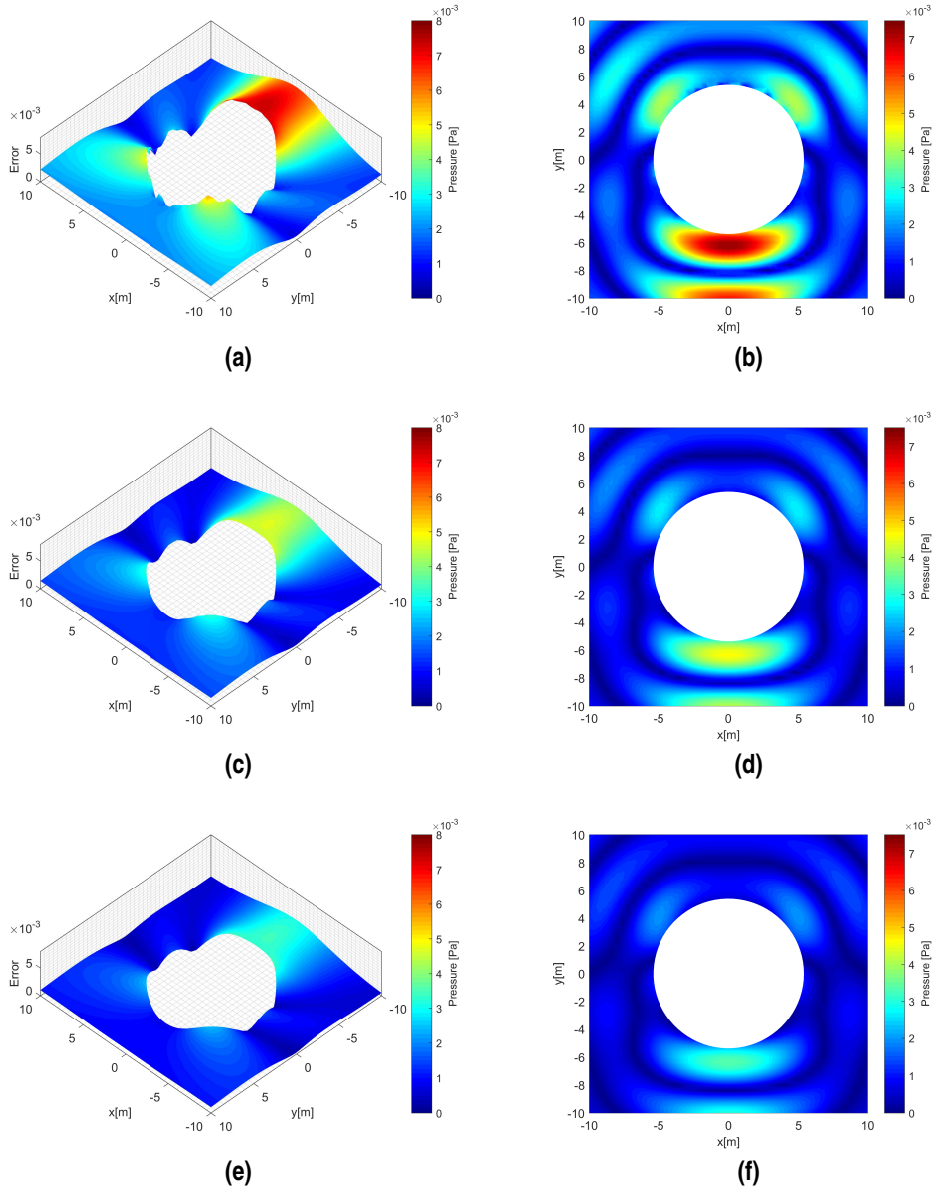

Figure 3.4 Absolute error obtained from discretizations (a-b) $1/h = 2/\pi\ m^{-1}$, (c-d) $1/h = 3/\pi\ m^{-1}$ and (f-g) $1/h = 4/\pi\ m^{-1}$.

Reference [10]. The element size in the second case varies from $h = 2.9$ mm to $h = 4.3$ mm, which means 805 nodes and 704 elements with 2415 degrees of freedom (Figure 3.5.(b)).

The computed results are compared with the reference solution [10]. Eight characteristic cross-sectional modes shapes were computed in the frequency range $0 - 6$ kHz. Four modes had axial/vertical displacement componets (Figure 3.6), while the rest were characterized by dominant lateral in plane vibrations of the cross-section (Figure 3.7). For the low frequency range, the computed results show a good agreement with reference solution, regadless of elements size. Some differences appear between numerical results and reference results for higher frequencies.

Furthermore, an analysis using spectral finite elements has been made. The cross-section has been represented by seven elements, three elements to model the railhead, three elements to model the foot and one element to model the neck. This is an advantage of the SEM, which allows to discretize the domain with fewer elements than the FEM. The problem was solved using different element order to assess the accuracy. Figure 3.8 shows the mesh with element order $p = 4$ and $p = 8$.

Computed results show a good agreement for most of the previously described waves. The lateral waves

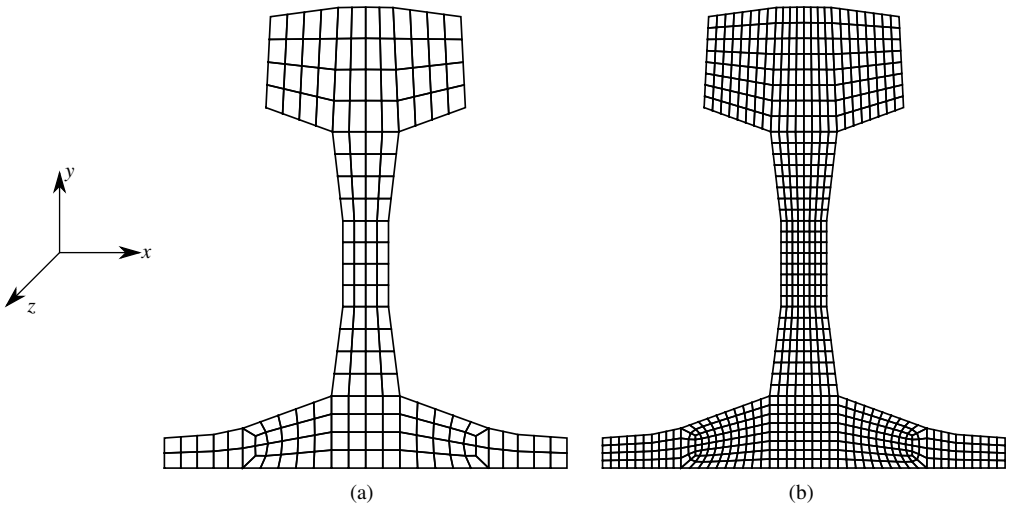

Figure 3.5 (a) Rail discretization for linear element size $h = 5.7 - 8.6$ mm elements and (b) $h = 2.9 - 4.3$ mm.

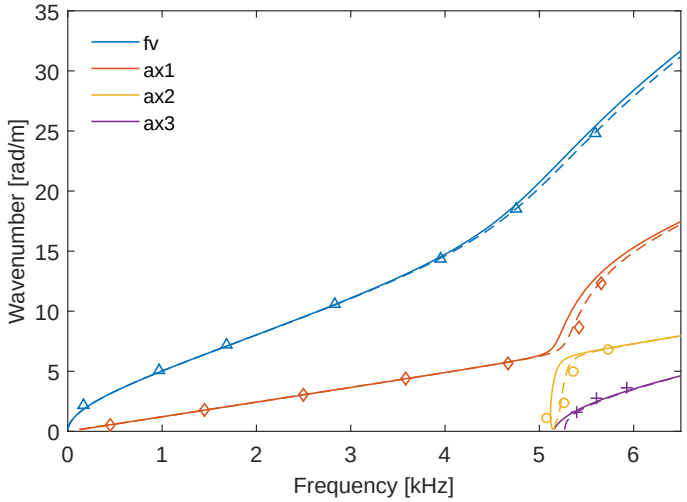

Figure 3.6 Dispesion curves of propagative vertical/longitudinal modes for the frequency range 0-6000 Hz. —, computed results for $h = 2.9 - 4.3$ mm; − −, computed results for $h = 5.7 - 8.6$ mm; △, ⋄, ○, +, reference results [10].

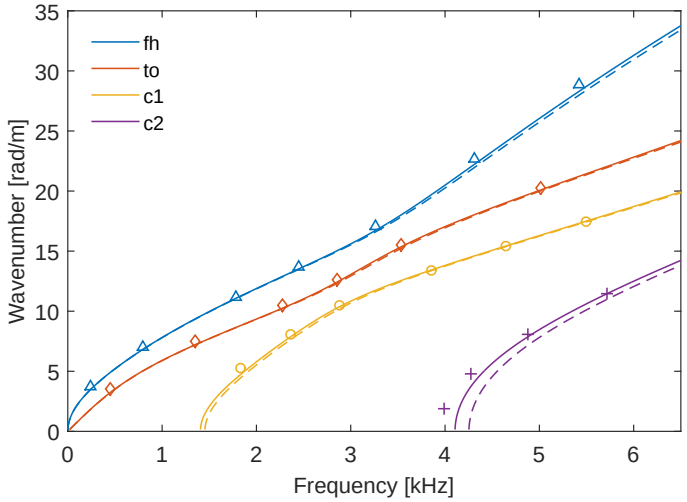

Figure 3.7 Dispesion curves of propagative lateral modes for the frequency range 0-6000 Hz. —, computed results for $h = 2.9 - 4.3$ mm; − −, computed results for $h = 5.7 - 8.6$ mm; △, ⋄, ○, +, reference results [10].

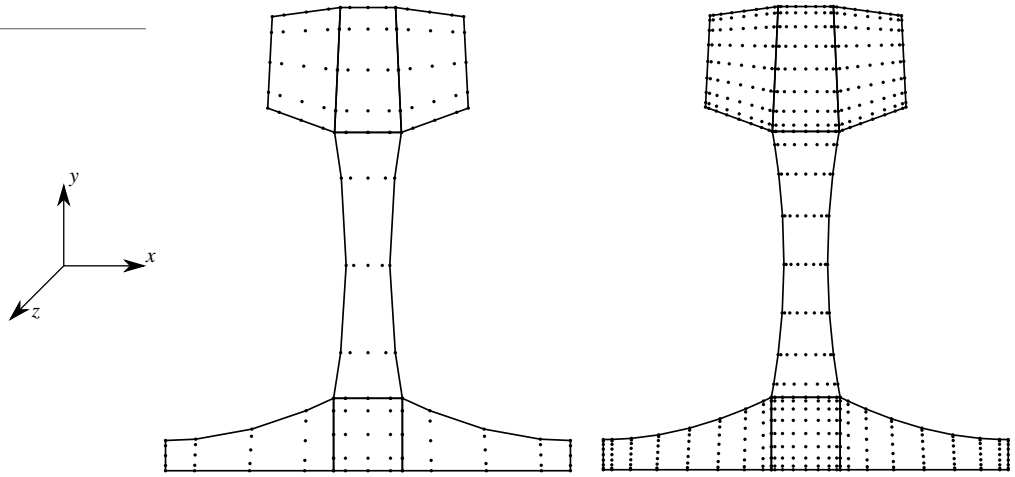

Figure 3.8 Rail discretization with spectral elements. Element order (a) $p = 4$ and (b) $p = 8$.

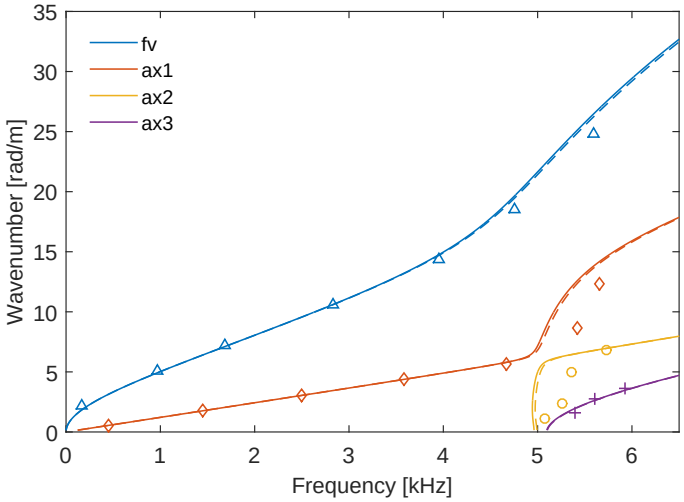

Figure 3.9 Dispesion curves of propagative vertical/longitudinal modes for the frequency range 0-6000 Hz. —, computed results for $p = 8$; − −, computed results for $p = 4$; △, ⋄, ○, +, reference results [10].

are quite similar to reference solution. Otherwise, axial curves denoted by $ax1$, $ax2$ and $ax3$ show appreciable differences with results presented in Reference [10] for the high frequencies. These differences could be explained by the coarse mesh used in Reference [10] for high frequencies. The proposed results in this work suggest that the solution for finer discretization converges to the SEM solution shown in Figures 3.9 and 3.10.

3.2.1 Axial waves in free rail

Figure 3.11 represents the displacement along the z axis due to the axial waves denoted by $ax1$, $ax2$ and $ax3$ for an excitation frequency of 5600 Hz. Despite these waves are axial in ther basic nature, the dominant movement of the cross-section at high frequencies is characterized foot flapping. The third axial wave ax3 presents a characteristic S-shape deformation of the cross-section.

3.2.2 Vertical bending waves of the free rail

Figure 3.12 shows the displacement along the y axis due to the vertical flexural wave fv. At low frequencies, this type of wave corresponds to simple beam flexion characterized by vertical translation of the undeformed cross-section during the wave propagation. As the frequency increases, the foot flapping becomes predominant.

3.2.3 Horizontal flexion of the free rail

Figure 3.13 shows the displacement along the x axis due to the horizontal flexural wave fh. Although is referred as horizontal flexion, it involves a small rotation of the cross-section, even at a very low frequency. This is due to the non-symmetry on the x axis of the rail profile. At low frequencies, the cross-section mainly

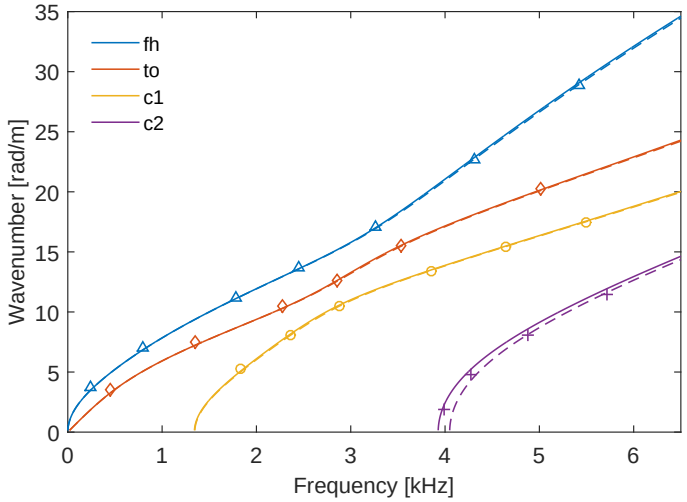

Figure 3.10 Dispesion curves of propagative lateral modes for the frequency range 0-6000 Hz. —, computed results for $p = 8$; − −, computed results for $p = 4$; △, ⋄, ○, +, reference results [10].

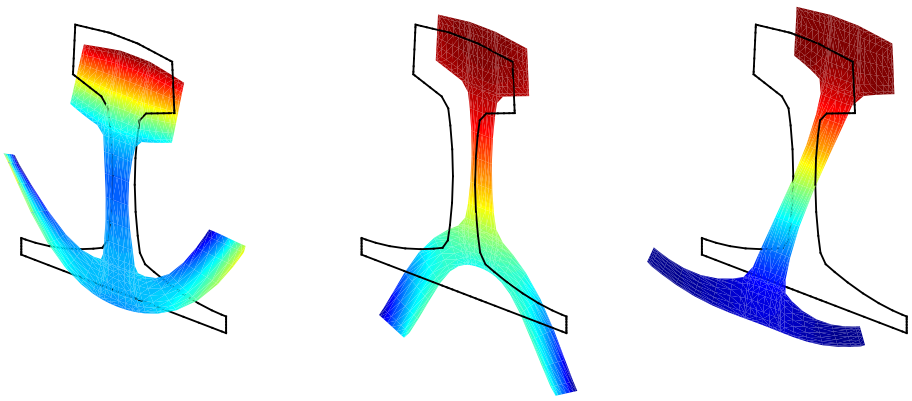

(a) **(b)** **(c)**

Figure 3.11 Axionometric representation of the cross-section modes of three axial waves at excitation frequency 5600 Hz; (a) $ax1$ wave, (b) $ax2$ wave, (c) $ax3$ wave.

translates horizontally as a rigid body. As the frequency increases, the feet rotation also increases and the neck of the profile starts to deform.

3.2.4 Torsion of the free rail

Figure 3.14 shows the mode of the cross-section due of torsional waves. At low frequencies the modal displacement can be characterized as a rigid body rotation of the cross-section. As frequency increases, the feet starts to vibrate more than the head, which leads to a deformation of the neck. At high frequencies the cross-secction presents a S in plane deformation.

3.2.5 Other types of propagative waves

The cross-section mode of propagative wave $c1$ and $c2$ cannot be described by using the analogies with simple beam waves. These two modes are characterized by the rotation of the head, by out-of-phase flapping of the feet and by deformation of the neck. The apparent increase of the dimesion of the hed of the rail is due to the graphical representation of the modal displacement, which are scaled to make the modes visible.

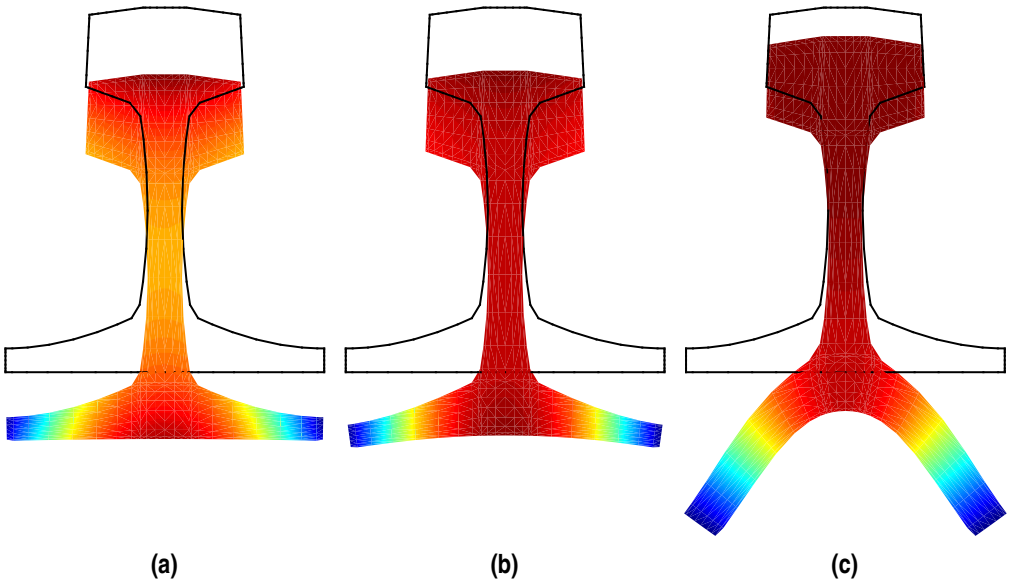

Figure 3.12 Front view of the cross-section mode of the vertical flexural wave fv at excitation frequencies (a) 450 Hz, (b) 1500 Hz and (c) 4200 Hz.

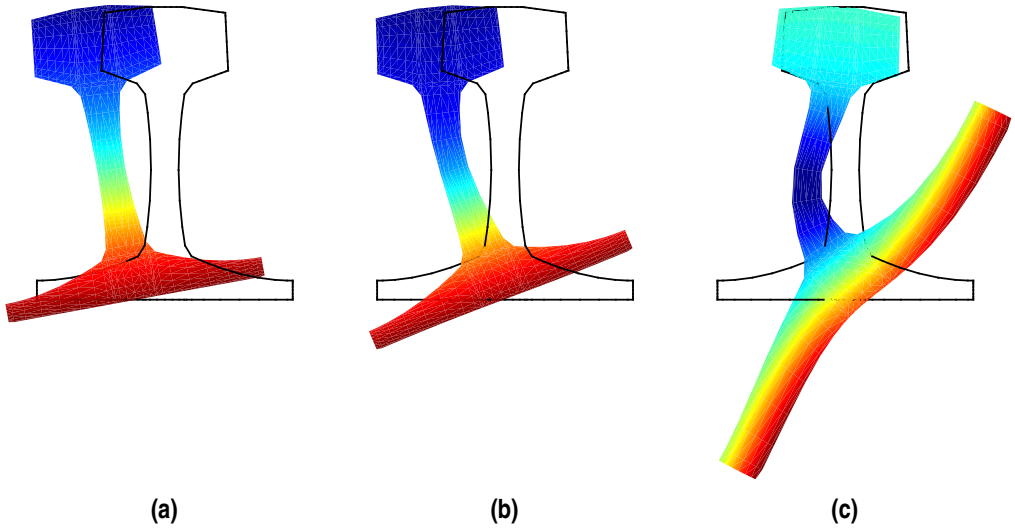

Figure 3.13 Front view of the cross-section mode of the horizontal flexural wave fh at excitation frequencies (a) 450 Hz, (b) 1500 Hz and (c) 4200 Hz.

These results are all in concordance with those described in Reference [10]. Therefore, the accuracy of the proposed method was verified.

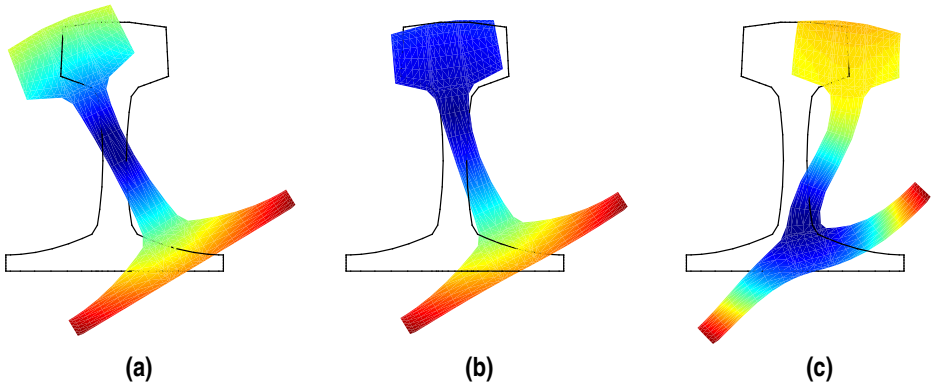

Figure 3.14 Front view of the cross-section mode of the torsional wave *to* at excitation frequencies (a) 450 Hz, (b) 1500 Hz and (c) 4200 Hz.

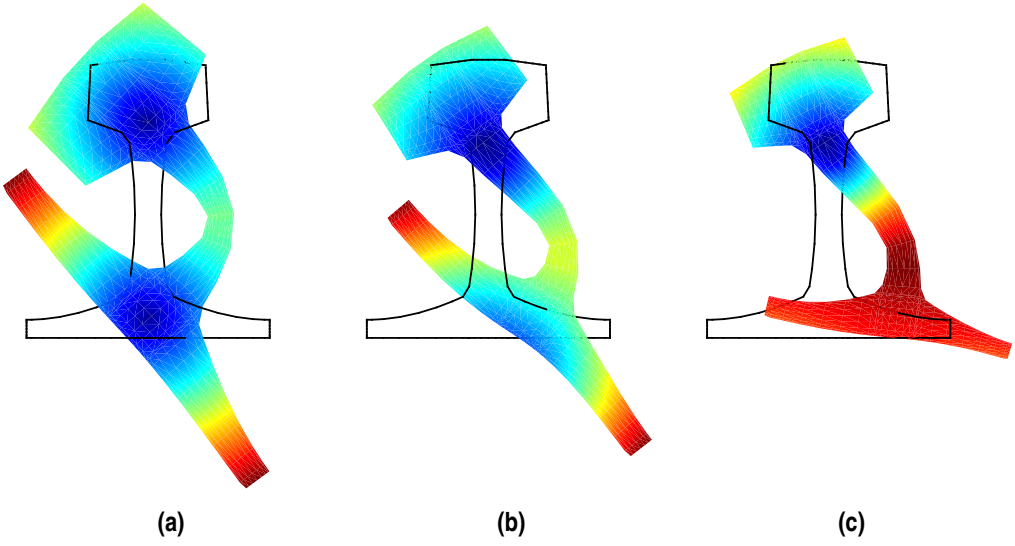

Figure 3.15 Front view of the cross-section mode of the propagative vawe $c1$ at excitation frequencies (a) 1500 Hz, (b) 2800 Hz and (c) 4200 Hz.

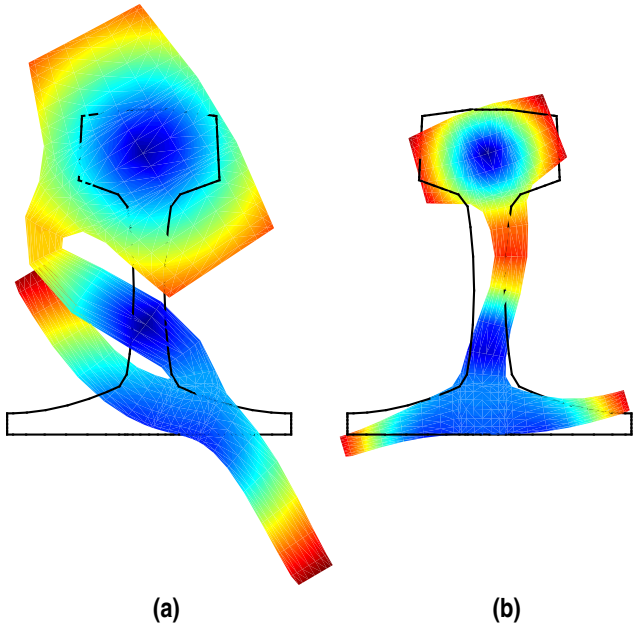

Figure 3.16 Front view of the cross-section mode of the propagative wave $c2$ at excitation frequencies (a) 4200 Hz and (b) 5200 Hz.

4 Conclusions and further developement

This work has proposed two spectral based formulations based on the FEM and the BEM to study fluid and solid wave propagation. Both models look at 3D problems whose materials and geometric properties remain homogeneous in one direction. Solid subdomain was modelled with the FEM, whereas the boundary of unbounded fluid media was modelled with the BEM. A spectral 2.5D FEM element for solid media and a spectral 2.5D BEM element for fluid-acoustics media were developed.

The models were verified with two benchmark problems with known solutions. The BEM was verified with a problem consisting of a cavity embedded in an unbounded fluid medium subjected to an incident wave field. The FEM was verified by computation the dispersion curves of propagative waves in free rail. Numerical results were in good agreement with the reference results.

Future researches should complete the work presented herein. The first step is improvement of the BEM model. This can be achieved by solving the singular integrals using more accurate methods, such as closed forms or a regularization procedure. The next step is to complete the coupling procedure in order to study fluid-solid interaction problems. Then, the radiated wavefield in an unbounded fluid medium caused by the deformation of a solid structure due to a point load can be studied.

List of Figures

Bibliography

[1] I. Babuška, F. Ihlenburg, E.T. Paik, and S.A. Sauter, *A generalized finite element method for solving the helmholtz equation in two dimensions with minimal pollution*, Computer Methods in Applied Mechanics and Engineering **128** (1995), no. 3-4, 325–359.

[2] I. Babuška and M. Suri, *P and H-P versions of the finite element method, basic principles and properties*, SIAM Review **36** (1994), no. 4, 578–632.

[3] P.Z. Bar-Yoseph, D. Fisher, and O. Gottlieb, *Spectral element methods for nonlinear spatio-temporal dynamics of an euler-bernoulli beam*, Computational Mechanics **19** (1996), no. 1, 136–151.

[4] H. Bériot, G. Gabard, and E. Perrey-Debain, *Analysis of high-order finite elements for convected wave propagation*, International Journal for Numerical Methods in Engineering **96** (2013), no. 11, 665–688.

[5] J. Biermann, O. von Estorff, S. Petersen, and C. Wenterodt, *Higher order finite and infinite elements for the solution of helmholtz problems*, Computer Methods in Applied Mechanics and Engineering **198** (2009), no. 13–14, 1171 – 1188.

[6] M. Bouchon and K. Aki, *Discrete wave-number representation of seismic source wavefields*, Bulletin of the Seismological Society of America **67** (1977), no. 2, 259–277.

[7] G. Degrande and G. De Roeck, *A spectral element method for two-dimensional wave propagation in horizontally layered saturated porous media*, Computers & Structures **44** (1992), no. 4, 717 – 728.

[8] A. Deraemaeker, I. Babuška, and P. Bouillard, *Dispersion and pollution of the fem solution for the helmholtz equation in one, two and three dimensions*, International Journal for Numerical Methods in Engineering **46** (1999), no. 4, 471–499.

[9] J. Domínguez, *Boundary elements in dynamics*, Computational Mechanics Publications and Elsevier Aplied Science, Southampton, 1993.

[10] L. Gavrić, *Computation of propagative waves in free rail using a finite element technique*, Journal of Sound and Vibration **185** (1995), no. 3, 531–543.

[11] F. Ihlenburg, *The medium-frequency range in computational acoustics: Practical and numerical aspects*, Journal of Computational Acoustics **11** (2003), no. 2, 175–193.

[12] F. Ihlenburg and I. Babuška, *Finite element solution of the helmholtz equation with high wave number Part I: The h-version of the FEM*, Computers and Mathematics with Applications **30** (1995), no. 9, 9–37.

[13] F. Ihlenburg and I. Babuška, *Finite element solution of the helmholtz equation with high wave number part II: the h-p version of the FEM*, SIAM Journal on Numerical Analysis **34** (1997), no. 1, 315–358.

[14] F. Ihlenburg, I. Babuška, and S. Sauter, *Reliability of finite element methods for the numerical computation of waves*, Advances in Engineering Software **28** (1997), no. 7, 417–424.

[15] P. Kudela, M. Krawczuk, and W. Ostachowicz, *Wave propagation modelling in 1d structures using spectral finite elements*, Journal of Sound and Vibration **300** (2007), no. 1–2, 88 – 100.

[16] O.Z. Mehdizadeh and M. Paraschivoiu, *Investigation of a two-dimensional spectral element method for helmholtz's equation*, Journal of Computational Physics **189** (2003), no. 1, 111 – 129.

[17] A.A. Oberai and P.M. Pinsky, *A numerical comparison of finite element methods for the helmholtz equation*, Journal of Computational Acoustics **08** (2000), no. 01, 211–221.

[18] A.T. Patera, *A spectral element method for fluid dynamics: Laminar flow in a channel expansion*, Journal of Computational Physics **54** (1984), no. 3, 468–488.

[19] S. Petersen, D. Dreyer, and O. von Estorff, *Assessment of finite and spectral element shape functions for efficient iterative simulations of interior acoustics*, Computer Methods in Applied Mechanics and Engineering **195** (2006), no. 44–47, 6463 – 6478.

[20] A.J.B. Tadeu and L.M.C. Godinho, *Three-dimensional wave scattering by a fixed cylindrical inclusion submerged in a fluid medium*, Engineering Analysis with Boundary Elements **23** (1999), no. 9, 745–755.

[21] A.J.B. Tadeu, P.F.A. Santos, and E. Kausel, *Closed-form integration of singular terms for constant, linear and quadratic boundary elements. Part 1. SH wave propagation*, Engineering Analysis with Boundary Elements **23** (1999), no. 8, 671–681.

[22] A.J.B. Tadeu, P.F.A. Santos, and E. Kausel, *Closed-form integration of singular terms for constant, linear and quadratic boundary elements. Part 2. SV-P wave propagation*, Engineering Analysis with Boundary Elements **23** (1999), no. 9, 757–768.

[23] P.E.J. Vos, S.J. Sherwin, and R.M. Kirby, *From h to p efficiently: Implementing finite and spectral/hp element methods to achieve optimal performance for low- and high-order discretisations*, Journal of Computational Physics **229** (2010), no. 13, 5161 – 5181.

[24] C. Zhu, G. Qin, and J. Zhang, *Implicit chebyshev spectral element method for acoustics wave equations*, Finite Elements in Analysis and Design **47** (2011), no. 2, 184 – 194.

[25] O.C. Zienkiewicz, *The finite element method*, third ed., McGraw-Hill, 1986.